Leveraging the Effect of Block Width during Infrared Neural Inhibition to Reduce Peak Temperatures

By

Jeremy Berlin Ford

Thesis

Submitted to the Faculty of the

Graduate School of Vanderbilt University

in partial fulfillment of the requirements

for the degree of

MASTER of SCIENCE

in

Biomedical Engineering

August 11, 2017

Nashville, Tennessee

Approved:

E. Duco Jansen, Ph.D.

Anita Mahadevan-Jansen, Ph.D.

ACKNOWLEDGMENTS

I would like to acknowledge the funding sources, which supported me and the equipment and supplies necessary for the completion of this work, including grants from the National Institutes of Health (NIH R56-NS087249, NIH R56-NS094651) and Air Force Office of Scientific Research (DOD/AFOSR FA9550-14-1-0303). I would like to thank my fellow lab members for their support in the research process, especially Mohit Ganguly for lending me his computational NEURON model for work within this thesis and for lending me his brain and his ears to bounce ideas off of. Additionally, I thank my collaborators at Case Western Reserve University (Dr. Michael Jenkins, Dr. Hillel Chiel, Emilie Lothet, Dr. Hui Lu, and Catherine Kehl) for their help in learning experimental setups, designing experiments, analyzing data, and everything slug. I would also like to thank my advisor, Dr. E. Duco Jansen, for his support and guidance. Last, I would like to thank all of those who aided me in the completion of this research through their support outside of the lab.

TABLE OF CONTENTS

LIST OF FIGURES

Figure Page

1. INTRODUCTION

1.1. Introduction to Thesis

Chronic pain has a diverse set of causes and can manifest in many forms. Typically brought on by neurological dysfunction or a painful stimulus, in many instances there is no simple cure. Globally 3-4.5% of the population suffers from neuropathic pain[1], pain arising from damaged or dysfunctional neural tissue, and accounting for a national economic burden of $560-635 billion[2]. While chronic pain can be indicative of some underlying problem, often times, especially after sustained exposure to a painful stimulus, the pain is no longer a symptom but becomes the disease. At this point, treatments rely on direct control of the neurons generating the neural pain signals. Clinical neuromodulation treatments primarily use either drugs which elicit systemic effects and carry the risk of habituation, tolerance, and addiction, or electric current which has a high cost barrier and tends to leak to adjacent tissues, limiting the spatial specificity of this technique. Other techniques which are either not standard clinically or are limited to research use include neuromodulation through ultrasonic and optical methods. Infrared neural inhibition (INI) is a spatially precise optical form of neural inhibition which does not require contact with the tissue. It is believed to function through neural heat block mechanisms, elicited by heating due to water's absorption of infrared (IR) light. While a threshold temperature rise is believed to be required for INI, the work in this Master's thesis suggests the importance of block width, or the distance of axon over which the heat is applied, in determining the temperature required for inhibition. Previous implementation of INI in *Aplysia californica* and rat nerves show acutely reversible conduction block without functional damage, however the noted temperature rises result in thermal loads [temperature * time] problematic for sustained clinical use. Methods to minimize this thermal load are required before there can be reliable, long-term utilization of INI. Assuming block width is an important factor in establishing the minimum temperature required for heat block, one way to reduce the maximum temperature experienced by tissue during INI is to distribute the heat over a greater length of axon, therefore reducing the thermal load at any individual point, and extending the possible application time of treatment. Therefore, this thesis introduces the first

experimental evidence that block width plays a role in dictating the maximum temperature rise required in the nerve at heat block threshold.

1.2. Background Materials

1.2.1 *Motivation*

The problem of chronic neuropathic pain is complex with many potential causes for the neurological dysfunction such as an underlying disease, injury, or over-sensitization of the pain pathway. Typical pain treatments rely on pharmaceuticals including opioids, however increasing evidence support the deleterious effects of prolonged opioid use, including abuse and overdose, and increased risk of fractures and myocardial infarctions[3,4]. The widespread use of opioids and ease of access to these drugs has increased their abuse which has become known as the opioid epidemic. The rate of overdose deaths involving opioids has nearly quadrupled since 1999 leading to opioids being associated with 6 of every 10 overdose deaths[5]. One of the problems is the over prescription of opioids, leading to the NIH Pain Consortium to put out a call for proposals for research into non-pharmaceutical pain-management[6]. Common non-pharmaceutical technologies to ameliorate peripheral neuropathies include transcutaneous electrical nerve stimulation (TENS) and spinal cord stimulation (SCS) which utilize transdermal injection of current or current injected through implanted electrodes. Currently these electrical stimulation devices are the standard of care for device-based pain treatments and provide adequate alleviation of pain. Their use is accompanied by a variety of potential complications and side effects over time. Drawbacks include lead migration, incompatibility with magnetic resonance imaging (MRI) scanners and pacemakers, relatively poor specificity, and paresthesia[7–12], however efforts are being made to overcome these limitations. Particularly with SCS, there is a high cost barrier and a 30-40% incidence of complications[12]. Conversely, optical methods have shown to be spatially precise and do not interfere with electrical recordings[13,14]. These techniques include infrared neural modulation (INM) which utilizes tissue's absorption of infrared light to control neuromodulation[13], optogenetics which genetically modifies neurons to express light-sensitive ion channels[15], and glutamate uncaging which uses chemically inactivated neurotransmitters with a photosensitive blocking group that is activated when light is applied[16]. These techniques do not rely on the use of

metal electrodes nor do they use the application of electric fields, thus their compatibility with pacemakers and MRI scanners is expected. Additionally, with their high spatial specificity, there is the potential for the development of novel methods of managing chronic neuropathic pain secondary to painful traumatic or disease related peripheral neuropathies (e.g. Complex Regional Pain Syndrome (CRPS), post-surgical neuropathies, diabetic peripheral neuropathy, phantom limb pain) that is associated with lower costs, good analgesic efficacy, and improved function without risks of dependency associated with opioid analgesics. Other methods for neuromodulation are available or are being explored but are not considered the standard of treatment, either due to a more niche implementation or due to their lack of clinical translation.

The neuromodulation capability of ultrasound was first published in 1929[17], and has since been used for both neural stimulation and inhibition[18,19]. Ultrasonic neuromodulation is non-invasive and has a large depth of penetration in tissue, thus is able to be implemented in transdermal and even transcranial fashions. However, when compared to more invasive techniques, this method provides relatively low spatial resolution neural modulation which limits its ability to control specific neural populations[18–20]. The underlying mechanism for ultrasonic neuromodulation is believed to be primarily mechanical, but other mechanisms cannot be ruled out as of yet. The true mechanism behind this technology has yet to be elucidated, and has become a complex question in the field[20].

Optical methods have emerged in the past few decades as potential mechanisms for modulating neural activity. In the 1980s direct illumination of neural tissue with visible/near infrared light was shown to elicit an effect[21–23]. While inhibition of pain signals was shown, the issue of tissue damage was not well addressed in these papers. Low level light therapy (LLLT) has also been applied for neural modulation by looking at the easing of pain[24]. Neurotransmitter uncaging is another method of optically modulating neurons. These caged molecules are signaling molecules which are inactivated by a photosensitive region of the molecule[16,25]. When exposed to light, the molecule becomes active and modifies neural activity. A common molecule used with this technique is glutamate due to its role in stimulating excitatory neurons. This technique has very high spatial resolution and has been used in neural circuit mapping experiments[26]. The most notable impact in recent years in the field of optical neuromodulation has been the development of optogenetics. Optogenetics uses implanted light sensitive ion channels in the membrane of target neurons[15]. By illuminating the tissue, neurons can be selectively excited or quieted.

Optogenetics began with channelrhodopsin which required blue light to activate and had its response saturate at relatively low frequencies. Since then, many types of optogenetic channels have been developed which allow for stimulation over a range of wavelengths and that can respond at high pulse frequencies[15]. Despite its utility, the main drawback of optogenetics is due to the genetic modification required to implant the ion channels in neurons. This poses a problem for clinical implementation and limits the use of optogenetics to research applications for the foreseeable future. More recently, infrared optical neuromodulation schemes have emerged. Questions still exist about the underlying mechanisms for these techniques, but they provide a spatially precise method which does not require introducing exogenous ion channels or agents, lending itself well for eventual clinical translation.

1.2.2 *Infrared Neural Modulation*

The field of neuroscience has known about the effect of temperature on neural signals since the early 1900's[27,28]. Hodgkin and Katz directly showed a change in *Loligo forbesi* neuron resting potential and action potential kinetics that was dependent upon the temperature of the surrounding media[28]. This effect has been utilized to employ heat block within nerves since at least the mid 1960's[29], and differential effects of heat on vertebrate fiber types has been noted since the 1980's[22]. Additionally, neural block resulting from cooling has been investigated extensively[30–32]. INI is another way of applying heat block which specifically allows for high spatial discrimination in a delivery scheme with highly customizable probes which do not require contact with tissue.

Direct optical modulation of neural tissue in the 1980's utilized light in the visible and near-infrared (NIR) wavelengths[23,33]. Many of these studies assessed pain inhibition. It was shown that, at least in one study, this irradiation resulted in inhibition of the neural signal but complete recovery of the signal was not possible, and sustained damage was noted when assessed days later[22]. In 2005, Wells *et al.* showed the first stimulation of action potentials using longer wavelengths (λ= 2.1-6.1 μm)[13]. This processes of optically stimulating neural tissue using infrared light was given the name infrared neural stimulation (INS). It was shown that the mechanism for INS is likely due to a spatio-temporal thermal gradient generated in the tissue due to water's direct absorption of light[34]. Therefore the main advantages of INS over other neuromodulation modalities are its spatial specificity, lack of reliance on exogenous agents, and ability to be applied without contact with the tissue. Application of INS has since been implemented at shorter wavelengths (λ=

1.4-2.1 μm) due to lower cost and miniaturization of laser sources at these wavelengths. Shapiro et al. investigated the underlying mechanism of INS by recording INS induced currents generated in different types of cell membranes while exposed to various channel blockers and showed how direct irradiation of any lipid bilayer using pulses of IR light results in capacitive currents[35,36]. Since this first set of experiments, INS has been tested in animal models ranging from *Aplysia* to humans and applied for motor control, stimulation of the cochlea, pacing of the heart, neural mapping, stimulation of the cavernous nerve, and stimulation of human dorsal rootlets, to name some of the applications[13,37–43]. Multiple methods of pairing INS with other techniques have been tested. Contrast enhanced methods using gold nanoparticles allow for the stimulating wavelength to be within the tissue optical window (800-1300 nm) but requires the introduction of exogenous particles to absorb those wavelengths[44–46]. Duke *et al.* explored the advantages of combining INS with electrical stimulation and found that the optical energy required for neural stimulation could be reduced while maintaining the increased spatial specificity[47–49].

In 2013, Duke *et al.* used INS wavelengths to elicit neural inhibition[14]. Due to the different effect on the tissue, this phenomenon was called infrared neural inhibition (INI). The initial study showed the utility of INI in both a vertebrate and an invertebrate model to inhibit AP generation, AP propagation, and muscle contraction[14]. Duke *et al.* reported an 8^{O}C rise associated with INI in the *Aplysia* buccal nerve and a 9^{O}C rise in the rat sciatic nerve. In contrast to previous optical inhibition studies, the neural signal immediately returned when irradiation ceased with no evidence of functional damage[14]. It is believed that INI works through heat block mechanisms, and that a temperature threshold is required as opposed to the spatio-temporal gradient needed in INS. By using a pulsed approach, heat is generated during irradiation of the tissue and thermal relaxation occurs during inter-pulse periods, and an overall temperature rise results from the superposition of the heating from multiple pulses. By controlling the laser parameters to modulate heating, temporal and spatial aspects of heating can be tailored, and phenomena inherent to INI induced heat block can be explored. Collaborators at Case Western Reserve University have described a size dependence whereby smaller axon diameters require lower laser radiant exposures and lower temperatures for block[50]. The work presented in this thesis will add to this knowledge by showing that block width plays an important role in the radiant exposure and peak temperatures necessary for INI[51]. These two phenomena will be leveraged in the future implementation of INI. The temperature rise described in Duke *et al.* are problematic for sustained implementation without

damage and pose a barrier to clinical use[14]. Therefore techniques are needed which minimize the temperature required for action potential block. The knowledge about block width and size dependence will guide the work performed to optimize the application of INI, and the work in this thesis will help provide the foundation for this knowledge.

1.2.3 *Laser-Tissue Interactions*

When laser light is incident on tissue, a number of interactions occur. First, some of the incident light is reflected off the tissue's surface due to the change in refractive index from either the glass-tissue interface (if the optical fiber is in contact) or the media-tissue interface (if the fiber is not in contact with tissue). The rest of the light is transmitted through the interface and into the tissue where scattering and/or absorption will take place. These interactions are typically defined by their wavelength dependent parameters, the absorption coefficient, μ_a [1/cm], and the scattering coefficient, μ_s [1/cm], as well as the anisotropy factor, g, which describes the directional tendency of scattered light. The mean path length before an absorption event occurs is $1/\mu_a$, while the mean path length before a scattering event occurs is $1/\mu_s$. The distribution of light within tissue can be estimated through different methods, however one of the most common and robust methods is through Monte Carlo simulations, a probabilistic approach which launches packets of photons into a tissue geometry and simulates photon paths using the radiative transport equation[52].

When considering INI, absorption events are important because they dictate the temperature rise within the nerve. When an absorption event occurs, a number of events can follow including heat generation, fluorescence, and the driving of photochemical reactions. In the case of INI, we are interested in heat generation not only because it's what drives heat block, but also because at these relatively long wavelengths (λ= 1.875μm in this thesis) photon energies are too low to drive photochemical reactions and there are no known fluorophores at this wavelength in tissue. The temperature rise (T) generated at a given spot in tissue is defined by:

$$T(x,y,z) = \frac{\mu_a H(x,y,z)}{\rho c_p} \tag{1}$$

where H(x,y,z) [J/cm^2] is the radiant exposure at the coordinates (x,y,z), ρ [kg/m^3] is the density of the tissue and c_p [J/kg/K] is the specific heat[52]. This equation assumes that the duration of the

laser pulse is sufficiently short compared to the thermal diffusion time constant of the tissue so that conduction during the laser pulse is negligible which is applicable when applying INI with 200μs pulse widths.

Once heat is generated, it can be dissipated through three possible means: conduction, convection, and radiation. Cooling of the tissue through radiation is typically ignored in these situations, therefore only conduction and convection will be considered here. Thermal conduction is the movement of heat down a spatial thermal gradient. The Fourier equation models the temperature time dependence of due to conduction[52].

$$\rho c_p \frac{dT}{dt} = k\nabla^2 T \tag{2}$$

where T is temperature and k is the thermal conductivity [W/m•K]. Convection is due to the relative motion between a fluid and substrate which are in contact and typically occurs in tissue due to blood perfusion. *In vitro* setups may have convection occur due to the movement of bath media over tissues. The heat flow due to convection at the tissue surface (Q_s [W]) is defined as:

$$\dot{Q}_s = hA(T_s - T_\infty) \tag{3}$$

where h is the convective heat transfer coefficient [W/m^2/K], A is the surface area at the interface [m^2], T_s is the surface temperature [K], and T_∞ is the bulk fluid temperature [K][52]. *In vivo* setups typically consider convection due to blood perfusion, and model this as a fraction of the volume being blood which is replaced with arterial blood at a set temperature, T_a. Time dependent temperature changes due to conduction and convection can be modeled together for tissue using the Pennes bioheat equation[52].

$$\rho c_p \frac{\partial T}{\partial t} = k\nabla^2 T + \omega_b \rho_b c_b (T_a - T) + \dot{Q}_{met} \tag{4}$$

where the subscript b denotes values for blood, ω_b is the rate of blood perfusion between arteries and veins per unit tissue mass [ml blood/ml tissues], and $\dot{Q}_{met}$ is the heat source term for metabolic heating. With a slight modification of the equation, we can account for the added heat from our

laser source, $\dot{Q}_{source}$ [W/m^3]:

$$\rho c_p \frac{\partial T}{\partial t} = k\nabla^2 T + \omega_b \rho_b c_b (T_a - T) + \dot{Q}_{met} + \dot{Q}_{source} \quad (5)$$

1.2.4 *Thermal measurements*

For this study, to confirm the effect of block width, the temperature rise must be quantified. There are a range of methods to measure temperature rise, however obtaining thermal data in tissue samples is a fundamental challenge with no perfect approach. Optimally, accurate spatial temperature maps in tissue at high spatial resolution and high temporal resolution could be achieved, however typically when optimizing for one parameter, there is a tradeoff in the other parameters. Thermocouples (TCs) are considered a gold standard for temperature measurements. They can be miniaturized for small regions of sensitivity and high temporal resolution. Their drawbacks are that only point measurements are possible, they can be very fragile when miniaturized, and they must physically be in contact with the region of interest which changes heating occurring at that spot as well as the entire thermal field. This can happen due to conduction of heat through the TC and by changing the boundary conditions of heating of the entire setup. Additionally, they have a relatively long response time and are susceptible to artifacts from direct laser irradiation. Thermal imaging is a technique which uses blackbody radiation emitted from the surface of the sample to calculate the sample's temperature. It can provide high spatial and temporal resolution temperature maps. Additionally, the method is non-contact so the sample does not need to be disturbed to take measurements. The drawback in biology is that tissue has a high water content and cameras are optimized for detection between either 3-5 μm or 8-12 μm. Due to the absorption coefficient of water at these wavelengths, the imaging depth is limited to 100 μm at most[53]. Therefore, only very superficial measurements in tissue can be taken, and only if the sample is not immersed in media. Magnetic resonance (MR) thermometry has been applied for monitoring temperature rise is tissue and is typically applied for guided ablation[54,55]. There are a few different methods to correlate different MR signals to temperature rise as overviewed in Rieke *et al.*[56]. MR thermometry allows for spatial temperature maps deep in tissue, and relatively high resolution voxels can be achieved at high magnetic field strengths. One drawback of this method

is its low temporal resolution, limiting measurements of laser heating during INI to steady state measurements. Additionally, MR scanners are costly and very high field strengths are required to achieve spatial resolutions necessary for monitoring laser heating during INI. Other temperature measurement techniques exist including but not limited to quantifying changes in florescence[57,58], Raman signal[59], and acoustic signals[60].

For this thesis, thermocouples proved to be optimal for characterizing the maximum temperature rise achieved during INI. Thermocouples are the junction of two metals which utilize the Seebeck effect to measure a change in temperature. The Seebeck effect is the thermal to electric energy conversion that can be visualized when considering a closed loop made from welding two different metals together (Figure 1A). In this configuration, a current will be generated which is proportional to the temperature difference between the two junctions formed[52]. Practically, an open loop configuration (Figure 1B) is used to measure temperatures whereby one of the junctions which serves as a reference node is held at a known temperature, called cold-junction-compensation, and another junction is used as a sensing node allowing absolute temperatures to be recorded. The thermocouple is then calibrated over its sensing range. Typically instead of holding the reference node at a known temperature for cold-junction-compensation, an electronic reference is used, measured using a thermistor or resistance temperature device, to determine the temperature of the reference node. By varying the two types of metals used in TCs, different temperature sensitivities and different applicable temperature ranges can be achieved[52]. Some common thermocouple types (metal/metal junction, sensitivity) are type T (Copper/Constantan, 42 μV/ºC), typeJ (Iron/Constantan, 53 μV/ºC), type K (Chromel/Alumel, 41 μV/ºC), and type E (Chromel/Constantan, 62 μV/ºC)[52]. Temporal resolution is dictated by the type of TC, the dimensions of the sensing junction, and the medium the TC is in[61]. If a TC, originally at temperature T_i, is placed in a region of ambient temperature, T_{inf}, the temperature of the TC, T, will approach T_{inf}, and the thermal time constant, τ, will be the length of time it takes for $\frac{(T-T_{inf})}{(T_i-T_{inf})} = \frac{1}{e}$. According to the lumped capacitance model, the time constant is can be solved for using the equation:

$$\tau = \frac{\rho V c}{h A_s} \tag{6}$$

where ρ is the density of the thermocouple, V is the volume of the sensing region, c is the specific heat of the thermocouple, h is the convective coefficient of the medium, and A_s is the surface area of the thermocouple. Depending on the use, thermocouple time constants can range from milliseconds to tens of seconds. For biological purposes, thermocouple wire sizes ranging from 10 μm to 100s of μms are used and time constants on the order of milliseconds to seconds are considered[52]. Wires at the probe tip are generally covered with a sheath such as Teflon or used in needles depending on the setting[52].

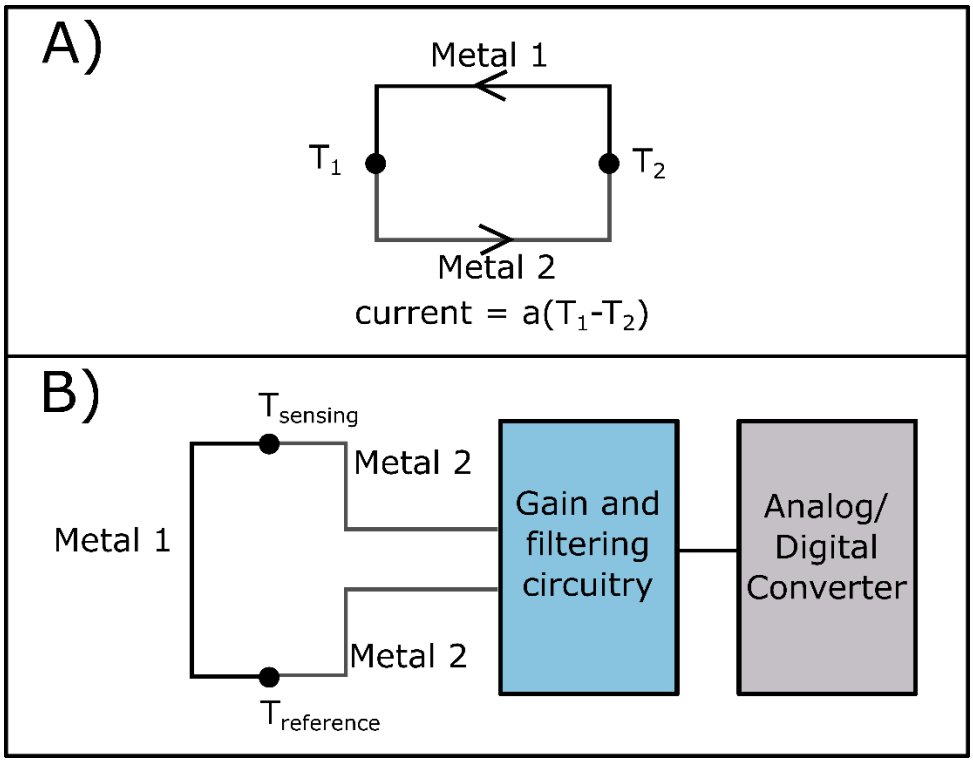

Figure 1. Thermocouple configurations. A) A closed loop of wire made from two separate metals welded together. Due to the Seebeck effect, thermal energy is converted to electric energy and a current flows in the loop which is proportional to the temperature difference between the two junctions. B) General thermocouple schematic using an open configuration of the wire loop from A. The temperature at $T_{sensing}$ is measured due to the other junction held at a reference temperature, T_{ref}.

1.2.5 *Temperature dependence of neurons*

In 1949, Hodgkin and Katz systematically showed the effect of different bath media temperatures on the resting potential and action potential dynamics of *Loligo forbesi* stellar nerves[28]. One important finding from this study was that action potentials failed around 40˚C but

returned when the nerves were returned to cooler temperatures. Thus, reversible heat block was shown. Since this important experiment, heat block has been studied in a range of animal and computational models. Different types of neurons have different thermal requirements for heat block[22]. Additionally, it has been shown that cooling of nerves can result in neural block, as well as can a mixture of both heating and cooling[30,32]. The current working hypothesis behind heat block suggests that repolarizing voltage-gated potassium channel (K_V) currents overwhelm the depolarizing voltage-gated sodium channel (Na_V) currents so that the action potential cannot be propagated in the adjacent region of axon membrane. This hypothesis stems from the following knowledge of temperature dependence in neural tissue.

When neural tissue is heated there are both changes in the resting state of the neurons and in the kinetics of ion channels. The steady state resting potential of cells depolarize in response to lower temperatures and hyperpolarize in response to high temperatures[62]. Carpenter *et al.* showed that while the while the resting potential of neurons decreased with increasing temperature, the threshold membrane potential to elicit an action potential was not temperature dependent[62]. Both K_V and Na_V peak currents increase at elevated temperatures[63]. The duration of these currents also decrease with increasing temperature. Additionally, K_V are more likely to be in a conducting state at lower voltages when temperatures are increased[63].

It has been shown that both sodium and potassium current amplitudes increase with temperature, however potassium currents have a greater temperature sensitivity[64–66] . Both sets of ion channels exhibit faster onset of currents at increased temperatures, but potassium onset times decrease in amplitude faster than sodium onset times[64–66]. The reason for this greater potassium channel sensitivity to temperature is likely due to K_V channels containing a region of amino acid residues similar to those found in TRPV1 (transient receptor potential subfamily V member 1) channels, a type of cation channel which can be gated by changes in temperature alone[65]. Recently, it was noted that pulsed infrared light can elicit a block of the propagation of neural signals in both vertebrate and invertebrate nerves[14]. It is believed that the mechanisms that dictate infrared neural inhibition (INI) are the same as those that are present in heat block. Because optical heating provides the ability to heat much smaller regions and change the width of heating by changing the spot size, questions about the relationship of threshold temperature vs both block width and axon diameter can now be asked. This raises the question of how the underlying mechanism facilitates these phenomena. Recently published work from Case Western Reserve University has developed

a mathematical analysis based on the cable equation of how the minimum block width required for INI scales with the square root of axon diameter[50,67]. The work in this thesis analyzes looks to demonstrate that an interplay exists between peak temperatures at inhibition and block width when axon diameter is unchanged. To help guide this process, computational models of neural activity can be used as described in the following section.

1.2.6 *Hodgkin-Huxley model*

The Hodgkin-Huxley (HH) model adequately represents the mechanism underlying action potential generation and propagation in neurons so that insight into changes in channel dynamics and ionic currents may be deduced. This model was introduced in a series of papers in the 1950s published by Hodgkin and Huxley[68,69]. The axon is modeled as a cylinder with a radius, r_i, and negligible membrane thickness. The extracellular space is assumed to be grounded and a good conductor. Currents through the membrane are defined as either an ionic current (I_{ionic}) or a capacitive current (I_{Cm}), whereby the total current through the membrane is the sum of the capacitive current and all ionic currents. The membrane is modeled as a capacitor (the membrane capacitance) and a set of parallel resistors and voltage sources (representing ion conductances and the Nernst potentials of individual ion species, respectively[68].

The HH model accounts for three types of ionic currents, sodium (Na^+), potassium (K^+), and leak (L) where:

$$I_{ionic} = I_{Na^+} + I_{K^+} + I_L \tag{7}$$

In Figure 4, each ionic current is dictated by an equilibrium potential, E_{ion}, and a conductance, g_{ion}. Variable conductances are used for Na^+ and K^+ to account for their voltage sensitivity. Each ionic current can be calculated as:

$$I_{ion} = g_{ion}(V_m - E_{ion}) \tag{8}$$

where V_m is the membrane potential. g_{Na} and g_K are modeled as a function of gating elements which represent the probability of the channel changing into either a conducting or non-conducting state: labeled m for sodium activation, h for sodium inactivation, and n for potassium activation.

Values for these gating elements were experimentally derived by monitoring sodium and potassium conductance over the course of the action potential. When fitting the change in potassium conductance, it was found that an n^4 relationship best modeled potassium activation. Similarly, sodium activation was found to have an m^3 relationship, and sodium inactivation an h relationship. Thus, conductance is modeled by the following equations:

$$g_{K^+} = \bar{g}_{K^+} n^4 \tag{9}$$

$$g_{Na^+} = \bar{g}_{Na^+} m^3 h \tag{10}$$

where $\bar{g}_{Na^+}$ and $\bar{g}_{K^+}$ are the maximum sodium and potassium conductance [conductance/cm^2], respectively, and n, m, and h are all dimensionless variables between 0 and 1. The gating elements n, m, and h can all be calculated from the equations:

$$\frac{dn}{dt} = \alpha_n (1 - n) - \beta_n n \tag{11}$$

$$\frac{dm}{dt} = \alpha_m (1 - m) - \beta_m m \tag{12}$$

$$\frac{dh}{dt} = \alpha_h (1 - h) - \beta_h h \tag{13}$$

where α and β are voltage dependent variables. α represents the rate of transfer for each gating variable from a non-activated state to an activated state, while β is the rate of transfer from an activated state to a non-activated state. Hodgkin and Huxley experimentally determined the values of α and β in the squid giant axon at 6.3^{O}C[68]. Both α and β values for other neural systems at other temperatures have been calculated[70,71]. A temperature dependence has been incorporated into these variables, deemed the Q_{10}. The Q_{10} is the rate by which biological processes are accelerated when their temperature increases by 10^{O}C, $Q_{10} = \frac{velocity\ at\ T_0+10}{velocity\ at\ T_0}$ [72].

Using the HH model, neural activity can be adequately modeled in response to a range of conditions such as tissue heating. This model can be implemented in NEURON, a simulation environment which provides a platform for computational models of neurons and networks of neurons, for ease of use. NEURON relies on the application of the cable equation:

$$\frac{\partial V}{\partial t} + I(V,t) = \frac{\partial^2 V}{\partial x^2} \tag{14}$$

which describes the current-voltage relationship in a one-dimensional cable[73]. Once a computational geometry has been set up, the cable equation can be applied at computational nodes and capacitive and ionic currents based on the HH model can be used to simulate neural activity. NEURON has been used to simulate neural activity in many scenarios, including for heat block[74]. One of the parameters able to be modified is the temperature of each computational node allowing for the simulation of INI with different block widths.

2. LEVERAGING THE EFFECT OF BLOCK WIDTH DURING INFRARED NEURAL INHIBITION TO REDUCE PEAK TEMPERATURES

2.1. Introduction

Infrared irradiation of excitable tissue has been utilized for both stimulation and inhibition of signal conduction[13,14,38,41,75–78]. Infrared neural stimulation (INS) has been utilized previously in our lab for stimulation of peripheral motor signals[37,79], the non-human primate visual cortex[75], rat somatosensory cortex[80], and human dorsal rootlets[39]. It has been shown that in the peripheral nervous system a transient spatiotemporal thermal gradient is required to stimulate activity[34] which is believed to create a transient capacitance change in the cell membrane leading to depolarizing currents[35,36], while central nervous system stimulation may function through alternate mechanisms[42]. Conversely, the mechanism underlying infrared neural inhibition (INI) is believed to be neural heat block which requires a sustained temperature rise[14]. INI is a method which leverages the use of laser light delivered through small diameter optical fibers, and tissue's absorption of infrared light, to create regions of increased temperature with high spatial discrimination. This results in a spatially precise approach for applying heat block. The first publication systematically showing the occurrence of heat block was published by Hodgkin and Katz in 1949[28]. It was noted that squid giant axons failed to conduct action potentials in the "vicinity of 40ºC", but the ability to conduct would return when the axon was cooled[28]. The hypothesized cellular mechanism is due to an increase in voltage gated potassium channel (K_V) currents with increasing temperature which arrests the action potential by counteracting the depolarizing currents of voltage gated sodium channels(Na_V)[14,28,64,65]. In the 1949 study, the entire bath media of the nerve was heated, however in the case of INI, only a small length of nerve is irradiated with infrared light, resulting in a localized temperature rise. Duke *et al.* measured this temperature rise to be ~8ºC during inhibition of *Aplysia californica* buccal nerve, and ~9ºC during INI of rat sciatic nerve, for absolute temperatures of ~30ºC and ~45ºC, respectively[14]. A computational study of heat block in *Xenopus laevis* predicts temperature rises up to 32ºC are required[74]. A recent study in the *Aplysia* buccal nerve estimates the required temperature rise during INI to be 10-15ºC, depending on the axon diameter of the neuron being inhibited[50]. These

predicted and measured temperature rises required for INI are likely problematic for sustained clinical implementation. Based on preliminary modeling in our lab, we hypothesize that the maximum temperature required during INI can be lowered by extending the length over which the neuron is heated (i.e. block width). This can be done by delivering the light through multiple optical fibers placed axially along the nerve. For this method to work, there must be an interaction between the block width and temperature needed for heat block, a relationship that has yet to be shown experimentally. Here, we show this relationship and present the relatively simple case of two adjacent optical fibers as a proof of concept of the impact of both block width on the temperature necessary to achieve INI.

2.2 Methods

2.2.1 *Computational Proof of Concept*

For an initial proof of concept of whether block width plays a role in the peak temperature required for INI, the response of an *Aplysia* pleural abdominal nerve axon to two different block widths was simulated. The Hodgkin-Huxley model implemented in the NEURON simulation environment was used for this. *Aplysia* neuron parameters were used in the simulation with an axon diameter of 2 μm which was 25 mm in length implemented over 9999 computational nodes. A temperature rise was applied to the axon which mimicked the temperature rise expected during INI. The shape of these temperature rises were guided by thermal camera (SC8303, FLIR Systems Inc., Wilsonville OR) temperature measurements of laser heating from optical fibers in 20% polyacrylamide gels with similar optical and thermal properties to that of tissue. First, an axon held at room temperature was simulated as a control to understand the neural conduction of a non-heated axon. The axon was stimulated by injecting electric current at the proximal node and the resulting propagation of the action potential down the axon was simulated, and the maximum membrane voltage of the action potential at each node was used to visualize the strength of the action potential. Next, the temperature increase due to heating from a single 400 μm core diameter optical fiber was applied along the axon. Inhibition was defined as a maximum membrane potential of < -40 mV at the most distal node. To find the temperature rise threshold associated with inhibition, the magnitude of the temperature profile along the nerve was modulated until the lowest temperature rise that resulted in inhibition was identified. A temperature profile approximating

heating due to two adjacent optical fibers was then applied to the axon and the temperature rise at inhibition threshold was identified using the same procedure as that for one optical fiber. As a control to show that this greater width of temperature rise results in lower peak temperatures at inhibition threshold, the temperature profile from one optical fiber was again applied such that the peak temperature in the profile equaled the peak temperature at inhibition threshold when using two fibers.

2.2.2 *Nerve Preparation*

Subsequent validation of the modeling results took place in the sea slug, *Aplysia califonica*. *Aplysia* (n=4, Marinus Scientific, Long Beach, CA) weighing 250-350g were anesthetized using injection of 333mM $MgCl_2$ (~50% of body weight). Once anesthetized, *Aplysia* were dissected and the pleural abdominal nerves were removed and pinned out in a recording dish lined with Sylgard (Dow Corning, Midland, MI), containing *Aplysia* saline (460 mM NaCl, 10 mM KCl, 22 mM MgCl, 33 mM $MgSO_4$, 10 mM $CaCl_2$, 10 mM glucose, 10 mM HEPES, pH ~7.6) at room temperature. Nerves were cut such that the cell bodies remained in the animal, thus the neural tissue utilized in this study is a bundle of unmyelinated axons. The nerve was then arranged as in Figure 2. Pinned nerve ends were cut and suctioned into hand-pulled polyethylene electrodes. Bipolar leads were used, terminating in chlorided silver wires. The positive end of the lead was placed into a suction electrode while the negative lead was placed in the saline bath. One electrode placed proximally on the nerve was used for electrical stimulation while the other was placed distally and used for recording. A custom optical probe made from two adjacent bare optical fibers (Figure 2) was placed in contact with the nerve between the stimulation and recording electrode. This probe was built in the lab using two bifurcated patch cords (Ocean Optics, Inc.). One channel from each patch cord was cleaved and the outer jackets were removed. The two bare fibers were secured parallel to each other using heat shrink tubing and epoxy and then polished together. Separation between adjacent claddings (~ 77μm) was determined using an infrared camera (FLIR SC8303, FLIR Systems Inc.) with 3.5 μm resolution. Each fiber had a cladding thickness of 20 μm, resulting in a separation distance of 117 μm between adjacent fiber cores.

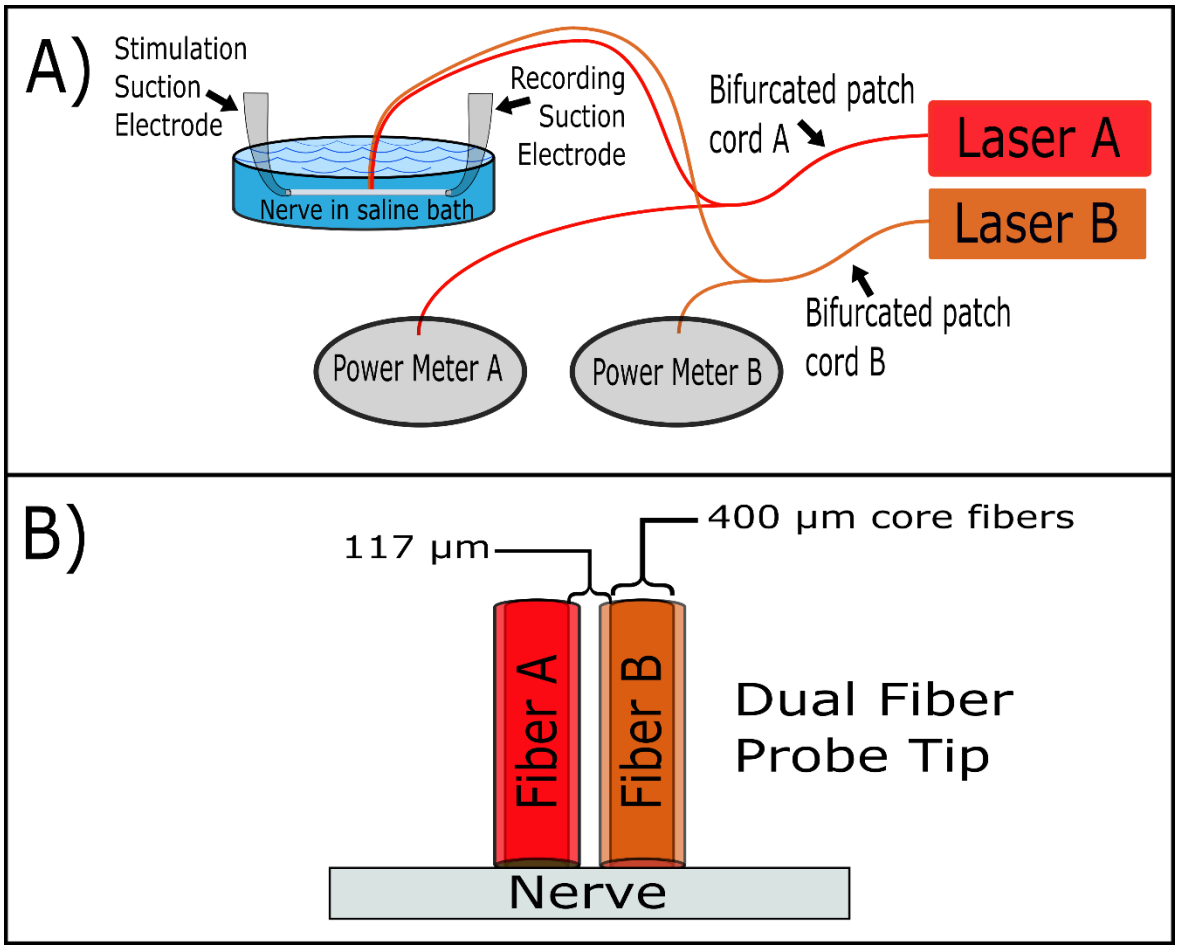

Figure 2. Experimental setup. A) *Aplysia* pleural-abdominal nerves were placed in a saline bath with suction electrodes for electrical stimulation and recording applied to the ends. A custom dual bifurcated fiber probe simultaneously delivered light from two different lasers (red and orange) to the nerve and to separate power meters for continuous monitoring of laser output power. B) Custom probe tip. One channel from each of the bifurcated fibers come together at the probe tip. Fiber core diameters are 400 µm with 20 µm thick claddings. The separation distance between the two cores was ~117 µm.

2.2.3 *Electrophysiological Recordings*

All recordings and triggering were performed using Axograph. Compound action potentials (CAPs) were stimulated at one end of the nerve using monophasic pulses of current (90-275 µA, 5 ms pulse width, 2 Hz, 90 second duration). The other end was used for bipolar recordings between the electrode and the bath media. Signals were amplified (10,000x) and filtered (Bandpass 100-1000 Hz) using a differential amplifier (A-M Systems, Model 1700), and digitized (Digidata 1440). Baseline recordings in which the lasers (λ= 1875 nm, Capella, Lockheed-Martin, Bothell

WA) were not triggered were first taken to establish normal behavior of the nerve in response to electrical stimulation. Next, radiant exposure thresholds required for inhibition were found using only one channel of the probe (fiber A). Electrical stimulation identical to that in a baseline recording was used, and laser A was triggered between 30 and 60 seconds (30 seconds off, 30 seconds on, 30 seconds off) at 200 Hz with 200 μs pulse durations. The radiant exposure at inhibition threshold using one fiber, H_1, was identified by slowly increasing the radiant exposure between recordings until inhibition of one of the CAP peaks was visualized. Once H_1 was identified, lasers A and B (200 μs pulse durations, 200 Hz) were triggered simultaneously to determine the inhibition threshold when using two optical fibers, H_2. Initially, the radiant exposure values out of each of the two optical fibers was set to 50% of H_1. Then, radiant exposures were slowly increased, keeping the radiant exposure out of fibers A and B equal. Inhibition threshold for two optical fibers was noted by the same criteria as for one optical fiber. Thus, the inhibition radiant exposure threshold for one fiber, H_1, and the inhibition radiant exposure threshold for two fibers, H_2, were identified.

2.2.4 *Thermocouple Recordings*

Thermocouple measurements were taken using a fine wire (12.7 μm diameter) type E thermocouple (FW05, Campbell Scientific, Logan UT) with a response time of ~1 ms, connected to a data acquisition device with cold-junction compensation (Model DI-245, DATAQ Instruments, Akron OH). The dual fiber probe was placed in a water bath, and the thermocouple was positioned under the probe at the hottest point using the following protocol. The laser was turned on and allowed to heat the water. Using a micromanipulator, the thermocouple was translated along all three axes until a maximum temperature value was found. Once the thermocouple was at this position of maximum temperature, the laser was turned off and the temperature was allowed to relax back to baseline (room temperature). The laser(s) was then triggered at 200 Hz with 200 μs pulses using a pulse generator (Model DG 535, Stanford Research Systems, Inc., Sunnyvale CA) mimicking the protocol used *in vitro*. Temperatures were allowed to reach steady state, which occurred well before the 30 seconds of irradiation used *in vitro*, so for clarity the data were analyzed once the temperature leveled off after 10 seconds of heating. This protocol was performed 3 separate times for each of the following setups: (1) the maximum temperature rise at H_1 was measured under fiber A, (2) the maximum temperature

under fiber A was measured when fibers A and B were both irradiating at H_2, (3) the maximum temperature under fiber B was measured when fibers A and B were both irradiating at H_2, (4) the maximum temperature rise at under fiber A was measured when only fiber A was irradiating at H_2.

2.2.5 *Data Analysis*

Compound action potentials (CAPs) were analyzed for identification of inhibition threshold radiant exposure for both one and two optical fibers. These signals result from the summation of the extracellular voltage of thousands of neurons. The rectified area under the curve (rAUC) is commonly used as a relative measure of the number of neurons contributing to the signal. If the rAUC is decreased, less neurons are contributing to the signal. For this reason, this metric is suitable for quantification of neurons in inhibition studies. To be more sensitive to inhibition of neural subpopulations, CAPs were split into separate regions over which to be analyzed. An artifact intrinsic to neural recordings is the activity dependent slowing of signal within a recording from repetitive stimulation of the axon[81]. Because of this artifact, analysis regions are susceptible to signal shift in which a reduction in rAUC may be due to signal shifting out of the analysis region and not due to INI. To mitigate this effect, the boundaries of these analysis regions were chosen as points of low variance across CAP signals for the 90 second recording (Figure 3) because these points experienced the least changes in signal and therefore the least signal shift. Three regions were used to analyze the response of different neural populations, separated by conduction velocity (CV). Region 1 was chosen to include the population of fastest CV neurons, while region 3 was chosen to include the population of slowest CV neurons. Region 2 contained the resulting area between regions 1 and 3 comprised of medium CV neurons. The boundaries of these regions were chosen as the local minima in the variance plot (Figure 3A) such that regions 1 and 3 fully encompassed the fastest and slowest set of CAP peaks, respectively (Figure 3B). This was performed for each recording. For each region, the rAUC was calculated and normalized to the largest rAUC of that region in the recording. For confirmation of inhibition, a two sample t-test was performed between the rAUC at time points before the laser was on and the rAUC of all time points suspected to exhibit inhibition. For example, the rAUC of region 3 of the representative pre-inhibition CAP in Figure 3B would be in the pre-laser irradiation group and the rAUC of region 3 in the representative inhibited CAP in Figure 3C would be in the group

suspected of exhibiting inhibition. A p-value of 0.05 was used as a threshold for significance. To assess differences between H_1 and H_2, a student's t-test was used. A p-value threshold of $p<0.05$ was imposed. For the temperature measurements, the three trials were averaged for each of the described setups. The steady state temperature rise value for fiber A at H_1 was compared to the steady state temperature for both of the two fiber scenarios using a student's t-test for each. A p-value threshold of $p<0.05$ was used.

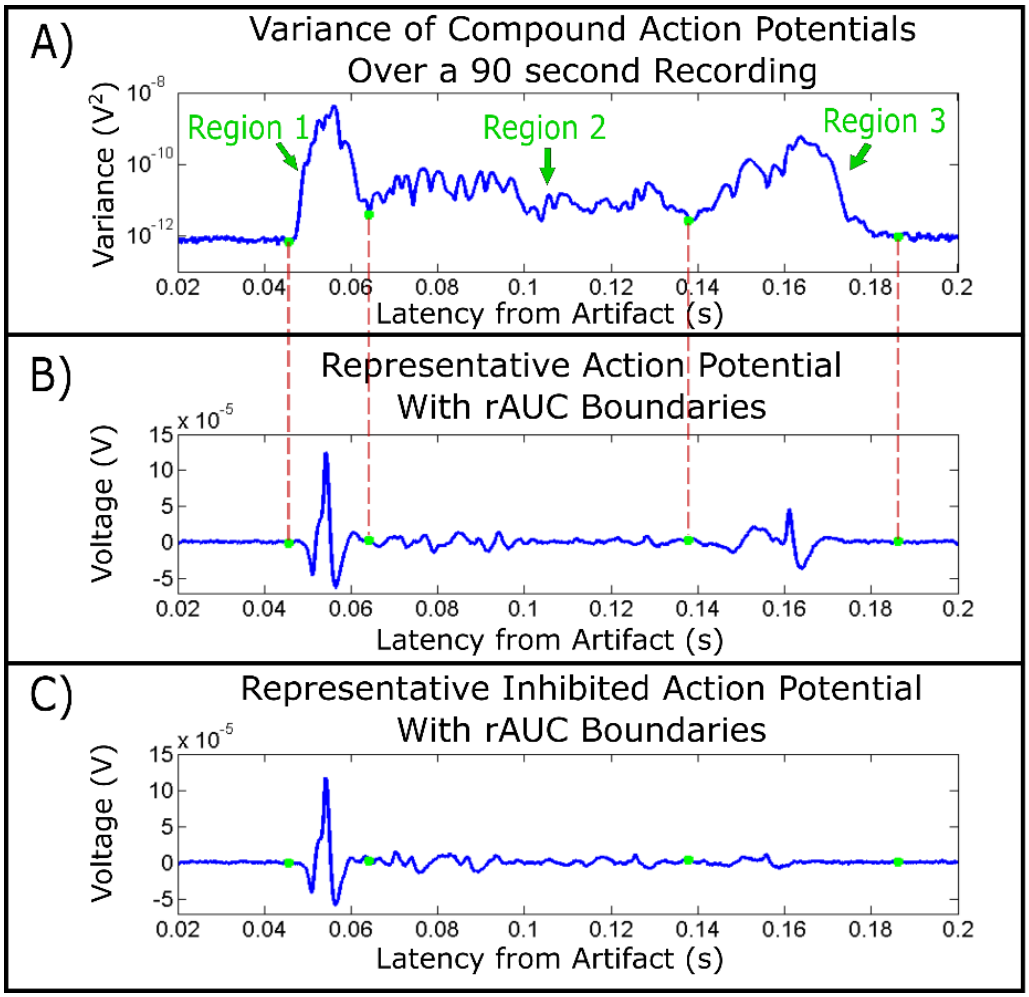

Figure 3. A) Variance of Compound Action Potentials (CAP) over an entire 90 second recording. Chosen region boundaries (green dots) are based upon points of low variance. B) A representative baseline CAP (before the laser is turned on) with low variance boundaries overlaid (green dots). C) A representative inhibited CAP (while the laser is turned on) with low variance boundaries overlaid (green dots).

2.3. Results

2.3.1 *Simulation Results*

Simulations of neural conduction suggested that with greater block widths, the peak temperature at inhibition threshold can be lowered. Figure 4 shows the resulting temperatures at inhibition threshold when applying temperature rises from laser heating setups using either one or two adjacent optical fibers. Column 1 shows the baseline neural conduction when the axon is held at room temperature (20.8^{o}C). It can be seen that there is a slight decrease in the maximum membrane potential as the action potential reaches the end of the axon. This is due to edge effects in the simulation, but does not affect conduction in the center of the axon. Next, temperature rises which mimic the expected temperature profiles from laser heating were then applied. It can be seen that a peak temperature rise of 24.2^{o}C above base temperature is necessary to elicit inhibition using a single optical fiber (Figure 4, column 2). Inhibition can be seen as the drop of the maximum membrane potential to the -65mV resting potential (Figure 4, column 2, bottom row). This peak temperature rise then drops to a 20^{o}C increase when heating from two adjacent fibers is applied (Figure 4, column 3), about a 17% reduction in the peak temperature. As a control, this 20^{o}C maximum temperature rise was applied using the one fiber temperature profile (Figure 4, column 4, top row). It can be seen that while the maximum membrane potential drops in the heated region, it then recovers and inhibition does not occur (Figure 4, column 4, bottom row).

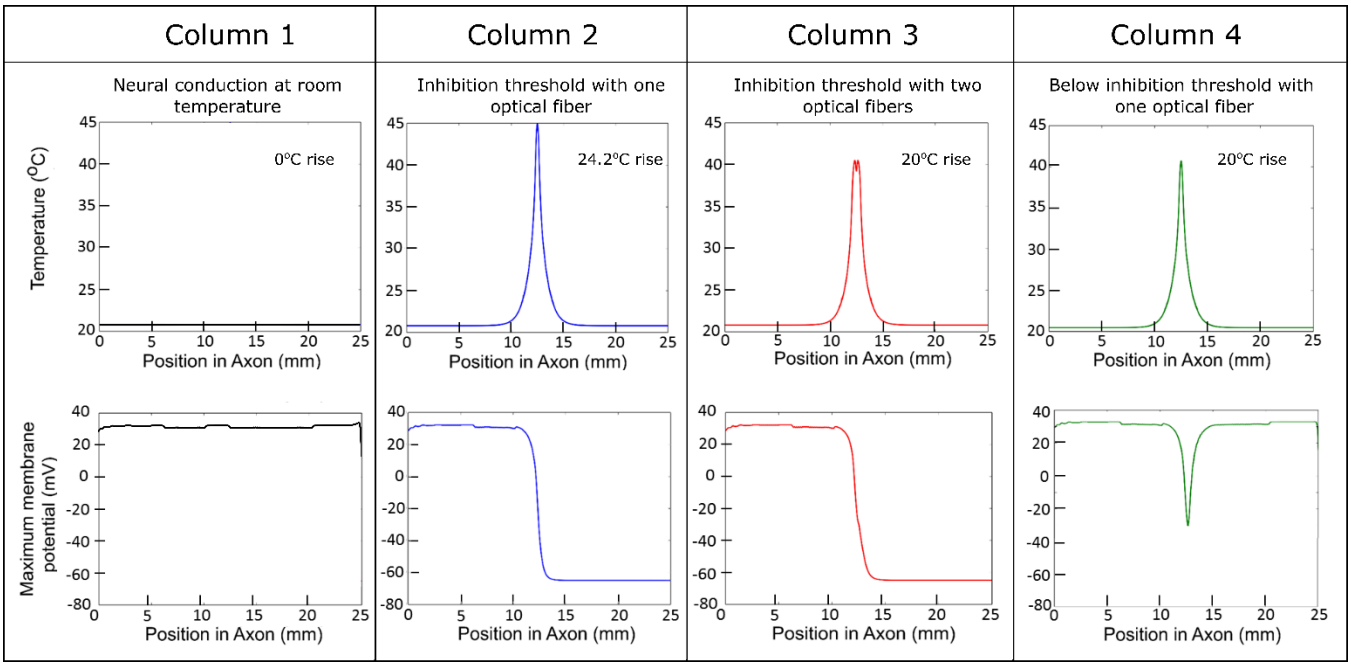

Figure 4. Computational proof of concept of block width through HH modeling of neural conduction at INI thresholds using one and two adjacent optical fibers. The model was applied to a room temperature baseline (column 1), the assumed heating profile from a single optical fiber at inhibition threshold (column 2), the assumed heating profiles from two adjacent optical fibers at inhibition threshold (column 3), and the assumed heating profile from a single optical fiber at the two fiber threshold peak temperature (column 4). The top row shows the temperature profile along the axon for each scenario. The bottom row shows the maximum membrane potential of the action potential at each computational node along the axon for each scenario.

2.3.2 *Radiant Exposure Thresholds*

Radiant exposure inhibition thresholds were found for both one, H_1, and two, H_2, fiber INI for each nerve. Rectified area under the curve calculations provided confirmation of inhibition. A representative response of the signal at inhibition can be seen in figure 8. Inhibition of the slowest set of neural populations is noted by a loss in the rAUC of region 3 (figure 5C) and confirmed using a two sample t-test between time points before the laser is on and when inhibition is suspected (values from 53-60 seconds in Figure 5C) ($p<0.05$). This method was applied to find the lowest radiant exposure at which there was a significant loss in rAUC, and that radiant exposure was defined as threshold. Resulting average values for H_1 and H_2 are shown in Figure 6. Single fiber inhibition threshold was found to be $H_1 = 169 \pm 8$ mJ/cm^2/pulse (mean ± standard deviation). Using two optical fibers resulted in a significant ($p<0.05$) drop in the inhibition threshold to H_2=

106 ± 12 mJ/cm^2/pulse. This corresponds to a ~37% reduction in radiant exposure when using two adjacent optical fibers.

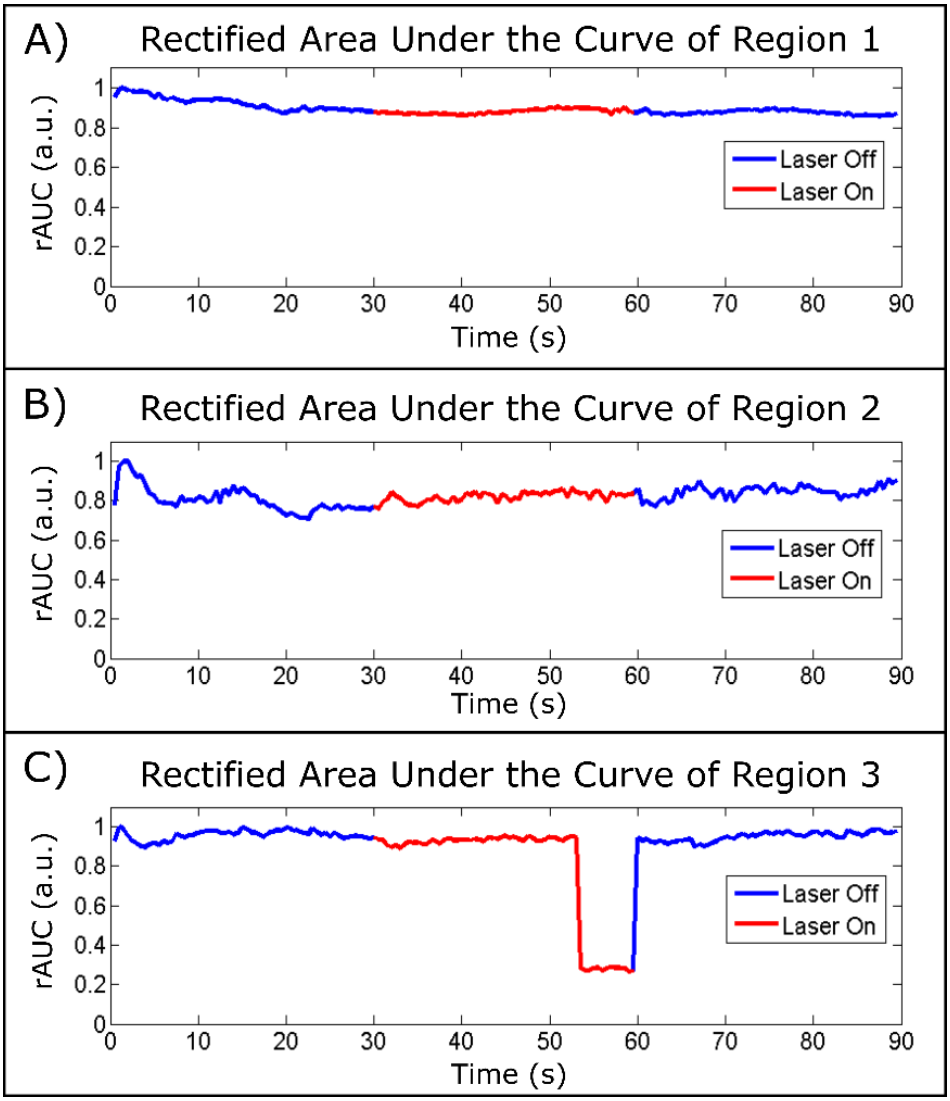

Figure 5. Rectified area under the curve (rAUC) plots for CAP regions in Figure 3: region 1 (A), region 2 (B), and region 3 (C). Note how selective inhibition of neural subpopulations in region 3 is visualized when the laser is on (red).

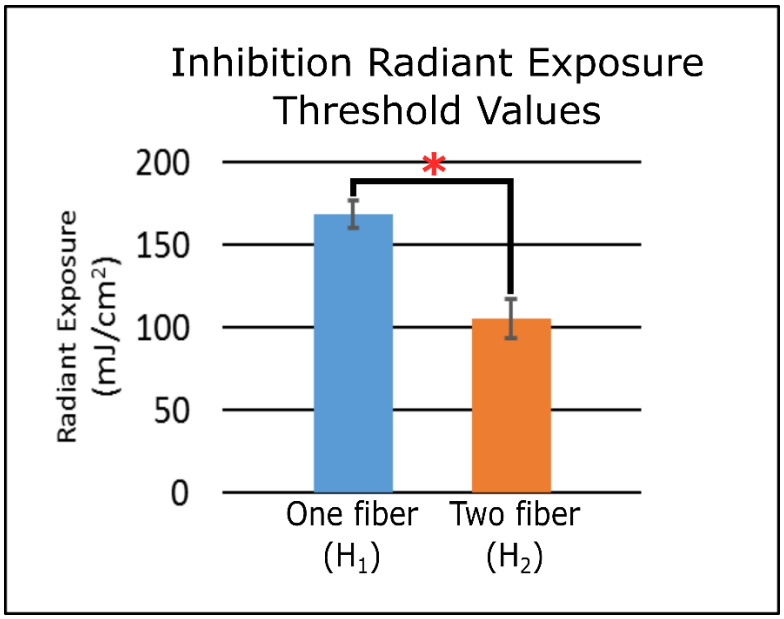

Figure 6. Radiant exposures required for inhibition using one or two optical fibers. * $p<0.05$.

2.3.3 *Temperature Rise at Inhibition Thresholds*

Due to the change in heating boundary conditions between one fiber and two fiber inhibition, temperature measurements are required to identify if increasing the block width of INI provides any thermal advantage. Preliminary modeling has shown that when the optical fiber is in contact with the nerve, the hottest point occurs at a depth (120-160 μm from the fiber output) within the tissue as opposed to superficially. Therefore, to access this point of maximum heating, maximum temperature rises associated with the laser heating at H_1 and H_2 were measured in a water bath to approximate temperatures reached *in vitro* in the slug nerve. With this setup, the distance between the tip of the probe and the thermocouple was able to be varied until the spot of maximum heating as found. While the thermal properties of water are different than nerve, they are on the same order of magnitude. Thus, if we assume that the optical properties of *Aplysia* nerve can be approximated as those of water at 1875 nm, while temperatures generated in water are expected to be similar to those in the slug, a slight underestimation of the exact temperature rise is expected in water due to water's higher thermal diffusivity than nerve, but similar trends are expected when heating with either one or two fibers. A fine wire TC was used (1) to minimize the effect of the presence of the thermocouple on the heating profile and (2) to be receptive to as small a volume as possible to measure as close to the maximum temperature. Temperature measurements

were taken at the average radiant exposure thresholds and averaged over three independent placements of the TC 10 seconds after the laser was turned on, once the temperature leveled out (Figure 7). While a rise of 17.8 ± 0.2 ºC (mean ± standard deviation) was noted for one fiber, this was able to be decreased to a temperature rise of 14.9 ± 0.2 ºC at the two fiber threshold value (black line Figure 7B), $p<0.05$. Notably about a 16% reduction. While it was originally expected that artifacts due to direct laser irradiation of the TC would be present and potentially obscure measurements, no laser artifacts were present in the recordings. This is likely due to that the calculated time constant of the thermocouple is around a millisecond or two in water while the sampling frequency of the data acquisition system was set to 200 Hz (5 ms time steps) so that laser induced transients could not be resolved.

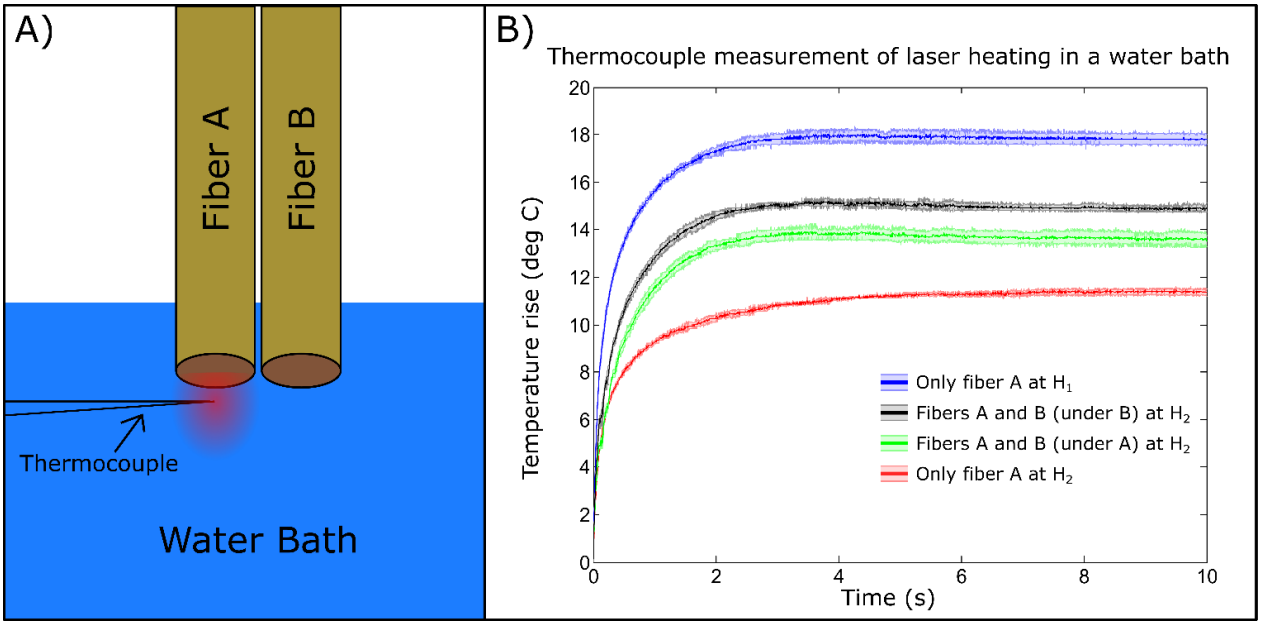

Figure 7. Temperature measurements at INI thresholds. A) Temperature recording setup where the probe tip is placed in a water bath and the thermocouple is placed at the hottest point below the fiber. B) Temperature rise due to laser irradiation (λ= 1875 nm, 200 µs pulse duration, 200 Hz). Temperature was measured (1) under fiber A when irradiating at H_1 (~169 mJ/cm^2/pulse) (Blue line), (2) under fiber A when both fibers A and B were irradiating at H_2 (~106 mJ/cm^2/pulse) (Green line), (3) under fiber B when both fibers A and B were irradiating at H_2 (Black line), and (4) under fiber A when only fiber A was irradiating at H_2 (Red line). For each setup, three separate trials were recorded with independent placement of the thermocouple for each trial. Each line is plotted as mean ± standard deviation.

2.4. Discussion

Both modeling and experimental data support that block width affects the temperatures required to achieve INI. Experimental results show a 37% reduction in the radiant exposure per fiber required for inhibition when two adjacent fibers are used compared to only one fiber. While any individual fiber may output less energy when using two fibers, there is still more total energy being deposited into the tissue, however, using two spots allows for a lower energy per volume. This parameter is important for its relationship to temperature rise from a single laser pulse, based upon the radiant exposure at the spot[52]. While radiant exposure can provide a guide to the temperature rise from an individual fiber, this is not the case as we move to more complex heating geometries. Therefore, we needed to take temperature measurements at the established radiant exposure thresholds. Precise thermal recordings in tissue pose a serious challenge. Thermocouples and thermistors require contact with tissue at the location of interest and can only record one point at a time and their mere presence change the heating dynamics in occurrence. Infrared imaging is a non-contact method that also provides spatial data about the thermal profile generated, but the drawback in tissue is its imaging depth. The absorption coefficient of water in the infrared region used by thermal cameras is high and therefore temperature sensing is limited to only a very superficial layer. When applying this to temperature monitoring for INI, the optical fibers can physically block the field of view of the camera and the maximum temperature rise occurs at a depth in the disuse greater than the camera can detect. Other methods for monitoring temperature such as temperature spatially offset Raman spectroscopy (TSORS)[59], the use of fiber Bragg gratings[82], and magnetic resonance thermometry[83] exist, but each has their respective advantages and drawbacks. Careful experimental planning must be made to adequately approximate the temperature being generated in the nerve during INI but no method exists which can perfectly measure this temperature. For our purposes, a method that could measure temperature at a depth in water with high spatial and temporal precision was required to be sensitive to the peak temperatures generated, and thus the fine wire thermocouple was chosen.

The thermal data show that the maximum temperature at inhibition threshold can be lowered by using two adjacent optical fibers for light delivery. Interestingly, the computational modeling predicted ~17% reduction in peak temperature at inhibition threshold and the thermal data shows ~16% reduction. This agreement supports that this type of simulation can be used to

make predictions about temperature's effect on neural conduction moving forward. One aspect to note here is that there is a slight disagreement between the steady state temperature under fibers A and B when both lasers are at H_2 (Figure 7B black and green lines). This discrepancy could be due to the interplay of multiple sources of variability in the system. First, there is an inherent variability to the output of the two lasers. It is possible that each diode can fluctuate slightly and actually be outputting slightly different radiant exposures when the temperature data was collected. More likely than this is that there can be coupling differences from the diodes to the optical fibers between the two laser systems. This would result in slightly different spot characteristics such as spot size and light distribution. If say fiber B had a slightly more confined energy density due to differences in coupling, it is possible that a higher temperature could be recorded under fiber B. Indeed, when this was investigated, it was noted that the coupling of light to the fibers was different between the two lasers and that fiber B had a slightly smaller spot size. Additional variations in temperature measurements can result from the placement of the thermocouple under the optical fibers. The temperature read out is highly dependent upon the exact location of the thermocouple in relation to the fiber output. The peak temperature will be found at a particular point within the thermal profile and temperatures fall off quickly outside of this point. Each of these sources of variability account for at least a few percentage points of error associated with each aspect of the temperature measurements (TC placement, light divergence differences, laser output, rounding errors), and collectively amount to ~10% error which likely explains the difference in the measured temperatures under fibers A and B at H_2. Important to note, however, is that despite this difference, both measured temperature rises are well below the temperature rise measured when using fiber A at H_1, supporting the original hypothesis that block width plays a role in INI. Moving forward, the temperature trends exhibited during this study can be used to guide our implementation of INI in safer ways, but damage measurements are necessary when the technique is applied to properly assess the safety.

In our investigation into the literature, we found no studies previously demonstrating the importance of block width during heat block. The underlying mechanism of heat block is believed to be due to changes in the dynamics of Na_V and K_V channels. It is believed that at increased temperatures the hyperpolarizing potassium currents overwhelm the depolarizing sodium currents and neurons are unable to reach the threshold voltage in the adjacent region of axon membrane required for propagation of the action potential. This is supported by the large temperature

sensitivity of voltage-gated potassium channels[65]. The temporal and spatial characteristics of voltages and currents in the axon can be analytically analyzed using the cable equation. For example, the NEURON model utilizes the cable equation to calculate voltage as a function of time and distance along an axon. Important to the understanding of the cable equation are the active and passive components of propagation of the action potential, which can be thought of as the axial currents along the axon. The active portion of action potential propagation is due to Na_V. The K_V are active but contribute to hyperpolarization. There is also a passive component of action potential propagation which would occur even in the absence of these voltage-gated channels, due to transmembrane leak currents, which is exemplified in the cable equation. When one solves for the time independent solution of passive propagation, it can be seen that the voltage exponentially decays as a function of distance due to membrane currents from membrane leak channels. This decay is based on the axon's length constant, defined as the length at which the voltage drops to 1/e of its original value, showing that there is a fixed distance over which this passive portion dies out.

It is conceivable that, due to the earlier onset and magnitude of K_V currents with temperature, at a certain temperature, T_1, the K_v hyperpolarizing current could exactly counteract the Na_V depolarizing currents, negating the active propagation of the action potential such that propagation is only passive. Consider this situation for a region of axon that is uniformly heated with an incoming action potential. When the action potential encounters the start of the heated region, the voltage would exponentially decay with distance due to passive propagation. For inhibition to occur, the width of any heated region must be long enough so that when the propagation encounters an unheated region which can support active propagation, the voltage has decayed to a point where Na_V are not triggered. Now consider that the heated region is heated to a temperature above T_1, called T_2. At T_1, active propagation is already being counteracted, but at T_2, K_V will have even greater hyperpolarizing currents, so how will this affect the propagation of the action potential? We can consider Kirchhoff's law which states that the sum of the currents flowing into a node must equal the sum of the currents flowing out of a node. If we take a cross section of axon in the heated region as a node, we see that the current flowing into that node is the incoming axial current of passive propagation, which is fixed based upon the axial current associated with a normal action potential. The currents out of the node are the outgoing axial current and the membrane current. At T_1, the net membrane current is equal to the leak current, but at T_2, the net

membrane current is the leak current plus some of the K_V current. Due to Kirchhoff's law, the outgoing axial current must be reduced. The membrane voltage will decay faster now due to the faster decay in axial current at T_2. The distance at which the Na_V can no longer be triggered will occur closer to the start of the heated region, and the width that needs to be heated for INI is decreased. Continuing to increase the temperature above T_2 will further reduce the block width required for INI. Therefore, the block width phenomenon is entirely due to the passive propagation of the action potential.

The ability to thermally manipulate neural tissue on a scale at which block width is important has emerged with the application of laser heating using small diameter optical fibers. While one may argue, why not heat the entire axon, the hypothesized mechanism as described above predicts that there will be no further reduction in temperature once the axon is heated at a particular block width. Additionally, when considering clinical implementation of INI, there is a feasibility limit to the length of nerve that can be manipulated. We postulate that laser heating may be an ideal modality to perform neural heating due to the development of laser diodes with relatively low cost, increasingly smaller size which can be worn on the body, and compatibility with pacemakers and electrical recording devices. By using an optical approach to neural heating, high spatial and temporal specificity can be leveraged for precise control over heating which can be optimized to reduce the thermal load during therapy.

2.5. Conclusions

In this thesis it was demonstrated that the block width over which heating is applied to neurons affects the temperature required to elicit heat block. This is important when implementing infrared neural inhibition in a therapeutic manner. The important metrics when predicting tissue damage is the temperature experienced and the duration of exposure. The results of this study demonstrate that the temperature required for INI can be modulated by tailoring the block width applied, opening the door to the optimization of different irradiation geometries for minimization of temperature rise which can be tailored to specific inhibition applications. Here, it has been shown that the temperature component can be modulated, but the duration of exposure can be optimized as well. Currently, we are using temperature as a stand-in for thermal damage, however when moving forward the damage must be quantified to assess

safety. While current temperature rises pose a barrier for clinical implementation of INI, the parameter space must be fully explored, as evidenced by the results of this thesis, before any final conclusions can be drawn about its clinical feasibility.

BIBLIOGRAPHY

1. Global Industry Analysts I. *Global Pain Management Market to Reach US$60 Billion by 2015, According to a New Report by Global Industry Analysts, Inc.* San Jose, CA; 2011. http://www.prweb.com/pdfdownload/8052240.pdf.
2. A. Pizzo P, M. Clark N, Carter Pokras O. *Relieving Pain in America: A Blueprint for Transforming Prevention, Care, Education, and Research*.; 2011. doi:10.3109/15360288.2012.678473.
3. Chou R, Turner JA, Devine EB, et al. The effectiveness and risks of long-term opioid therapy for chronic pain: A systematic review for a national institutes of health pathways to prevention workshop. *Ann Intern Med*. 2015;162(4):276-286. doi:10.7326/M14-2559.
4. Vowles KE, McEntee ML, Julnes PS, Frohe T, Ney JP, van der Goes DN. Rates of opioid misuse, abuse, and addiction in chronic pain: a systematic review and data synthesis. *Pain*. 2015;156(4):569-576. doi:10.1097/01.j.pain.0000460357.01998.f1.
5. US Department of Health and Human Services. *The Opioid Epidemic: By the Numbers*.; 2016. https://www.hhs.gov/sites/default/files/Factsheet-opioids-061516.pdf.
6. NIH Pain Consortium. NIH-DoD-VA Pain Management Collaboratory Funding Opportunity Announcement. 2016. https://grants.nih.gov/grants/guide/rfa-files/RFA-AT-17-002.html.
7. Liebano R, Rakel B, Vance CGT, Walsh DM, Sluka K a. An Investigation of the Development of Analgesic Tolerance to Transcutaneous Electrical Nerve Stimulation (TENS) in Humans. *Pain*. 2011;152(2):335-342. doi:10.1016/j.pain.2010.10.040.An.
8. Jones I, Johnson MI. Transcutaneous electrical nerve stimulation. *Contin Educ Anaesthesia, Crit Care Pain*. 2009;9(4):130-135. doi:10.1093/bjaceaccp/mkp021.
9. Bergeron-Vézina K, Corriveau H, Martel M, Harvey M-P, Léonard G. High- and low-frequency transcutaneous electrical nerve stimulation does not reduce experimental pain in elderly individuals. *Pain*. 2015;156(10):2093-2099. doi:10.1097/j.pain.0000000000000276.
10. Grider JS, Manchikanti L, Carayannopoulos A, et al. Effectiveness of Spinal Cord Stimulation in Chronic Spinal Pain: A Systematic Review. *Pain Physician*. 2016;19(1):E33-E54.
11. Moore DM, McCrory C. Spinal cord stimulation. *BJA Educ*. 2016:1-6. doi:10.1053/trap.2000.9683.
12. Verrills P, Sinclair C, Barnard A. A review of spinal cord stimulation systems for chronic pain. *J Pain Res*. 2016;9:481-492. doi:10.2147/JPR.S108884.
13. Wells J, Kao C, Jansen ED, Konrad P, Mahadevan-Jansen A. Application of infrared light for in vivo neural stimulation. *J Biomed Opt*. 2005;10(6):64003. doi:10.1117/1.2121772.
14. Duke AR, Jenkins MW, Lu H, McManus JM, Chiel HJ, Jansen ED. Transient and selective suppression of neural activity with infrared light. *Sci Rep*. 2013;3:2600. doi:10.1038/srep02600.
15. Deisseroth K. Optogenetics: 10 years of microbial opsins in neuroscience. *Nat Neurosci*. 2015;18(9):1213-1225. doi:10.1038/nn.4091.
16. Pettit DL, Wang SSH, Gee KR, Augustine GJ. Chemical two-photon uncaging: A novel approach to mapping glutamate receptors. *Neuron*. 1997;19(3):465-471. doi:10.1016/S0896-6273(00)80361-X.
17. Harvey EN. The effect of high frequency sound waves on heart muscle and other irritable tissues.

Am Heart J. 1929;5(3):388. doi:10.1016/S0002-8703(30)90343-2.

18. Tyler WJ, Tufail Y, Finsterwald M, Tauchmann ML, Olson EJ, Majestic C. Remote Excitation of Neuronal Circuits Using Low- Intensity, Low-Frequency Ultrasound. *PLoS One*. 2008;3(10). doi:10.1371/journal.pone.0003511.
19. Legon W, Sato TF, Opitz A, et al. Transcranial focused ultrasound modulates the activity of primary somatosensory cortex in humans. *Nat Neurosci*. 2014;17(2):322-329. doi:10.1038/nn.3620.
20. Naor O, Krupa S, Shoham S. Ultrasonic neuromodulation. *J Neural Eng*. 2016;13(3):31003. doi:10.1088/1741-2560/13/3/031003.
21. Gysbrechts B, Wang L, Trong NN, et al. Light distribution and thermal effects in the rat brain under optogenetic stimulation. *J Biophotonics*. 2016;9(6):576-585. doi:10.1002/jbio.201500106.
22. Klumpp D, Zimmermann M. Irreverisble differential block of A- and C-fibres following local nerve heating in the cat. *J Physiol*. 1980;298(1):471-482. doi:10.1113/jphysiol.1980.sp013095.
23. Walker J. Relief from chronic pain by low power laser irradiation. *Neurosci Lett*. 1983;43(2-3):339-344. doi:10.1016/0304-3940(83)90211-2.
24. Sushko BS, Lymans'kyi IP, Huliar SO. [Action of the red and infrared electromagnetic waves of light-emitting diodes on the behavioral manifestation of somatic pain]. *Fiziol Zh*. 2007;53(3):51-60.
25. Kantevari S, Matsuzaki M, Kanemoto Y, Kasai H, Ellis-Davies GCR. Two-color, two-photon uncaging of glutamate and GABA. *Nat Methods*. 2010;7(2):123-125. doi:10.1038/nmeth.1413.
26. Shepherd GMG. Circuit mapping by ultraviolet uncaging of glutamate. *Cold Spring Harb Protoc*. 2012;7(9):998-1004. doi:10.1101/pdb.prot070664.
27. Bernstein J. Untersuchungen zur Thermodynamik der bioelektrischen Ströme. *Pflugers Arch Eur J Physiol*. 1902;92(10-12):521-562. doi:10.1007/BF01790181.
28. Hodgkin AL, Katz B. the Effect of Temperature on the Electrical Activity of the Giant Axon of the Squid. *J Physiol Lucas Gasser Schoepfle Erlanger Cardot Arvanitaki*. 1949;9:240-249.
29. Letcher FS, Goldring S. The effect of radiofrequency current and heat on peripheral nerve action potential in the cat. *J Neurosurg*. 1968;29(1):42-47. http://thejns.org/doi/abs/10.3171/jns.1968.29.1.0042?url_ver=Z39.88-2003&rfr_id=ori:rid:crossref.org&rfr_dat=cr_pub%3Dpubmed.
30. Douglas WW, Malcolm JL. The effect of localized cooling on conduction in cat nerves. *J Physiol*. 1955;130(1):53-71. https://www.ncbi.nlm.nih.gov/pmc/articles/PMC1363452/.
31. Franz DN, Iggo A. Conduction failure in myelinated and non-myelinated axons at low temperatures. *J Physiol*. 1968;199(2):319-345. doi:10.1113/jphysiol.1968.sp008656.
32. Zhang Z, Lyon TD, Kadow BT, et al. Conduction Block of Mammalian Myelinated Nerve by Local Cooling to 15-30 °C after a Brief Heating. *J Neurophysiol*. 2016;115(3):1436-1445. doi:10.1152/jn.00954.2015.
33. Rochkind S, Nissan M, Lubart R, Avram J, Bartal A. The in-vivo-nerve response to direct low-energy-laser irradiation. *Acta Neurochir (Wien)*. 1988;94(1-2):74-77. doi:10.1007/BF01406620.
34. Wells J, Kao C, Konrad P, et al. Biophysical Mechanisms of Transient Optical Stimulation of Peripheral Nerve. *Biophys J*. 2007;93(7):2567-2580. doi:10.1529/biophysj.107.104786.
35. Shapiro MG, Homma K, Villarreal S, Richter C-P, Bezanilla F. Infrared light excites cells by changing their electrical capacitance. *Nat Commun*. 2012;3:736. doi:10.1038/ncomms1742.

36. Plaksin M, Kimmel E, Shoham S. Thermal transients excite neurons through universal intramembrane mechano-electrical effects. *bioRxiv*. 2017. http://biorxiv.org/content/early/2017/02/25/111724.abstract.

37. Wells JD, Thomsen S, Whitaker P, et al. Optically mediated nerve stimulation: Identification of injury thresholds. *Lasers Surg Med*. 2007;39(6):513-526. doi:10.1002/lsm.20522.

38. Richter C-PP, Matic AI, Wells JD, Jansen ED, Walsh JT. Neural stimulation with optical radiation. *Laser Photonics Rev*. 2011;5:68-80. doi:10.1002/lpor.200900044.

39. Cayce JM, Wells JD, Malphrus JD, et al. Infrared neural stimulation of human spinal nerve roots in vivo. *Neurophotonics*. 2015;2(1):15007. doi:10.1117/1.NPh.2.1.015007.

40. Tozburun S, Hutchens TC, McClain M a, Lagoda G a, Burnett AL, Fried NM. Temperature-controlled optical stimulation of the rat prostate cavernous nerves. *J Biomed Opt*. 2013;18:67001. doi:10.1117/1.JBO.18.6.067001.

41. Fried NM, Lagoda G a, Scott NJ, Su L-M, Burnett AL. Noncontact stimulation of the cavernous nerves in the rat prostate using a tunable-wavelength thulium fiber laser. *J Endourol*. 2008;22(3):409-413. doi:10.1089/end.2008.9996.

42. Cayce JM, Friedman R, Roe AW, Konrad PE, Jansen ED, Mahadevan-Jansen A. Relating optical signals induced by infrared neural stimulation to electrophysiology. In: *Proceedings of the 2010 Biomedical Science and Engineering Conference, BSEC 2010: Biomedical Research and Analysis in Neuroscience, BRAiN*.; 2010. doi:10.1109/BSEC.2010.5510836.

43. Jenkins MW, Wang YT, Doughman YQ, Watanabe M, Cheng Y, Rollins AM. Optical pacing of the adult rabbit heart. *Biomed Opt Express*. 2013;4(9):1626-1635. doi:10.1364/BOE.4.001626.

44. Sordillo LA, Pu Y, Pratavieira S, Budansky Y, Alfano RR. Deep optical imaging of tissue using the second and third near-infrared spectral windows. *J Biomed Opt*. 2014;19(5):56004. doi:10.1117/1.JBO.19.5.056004.

45. Eom K, Kim J, Choi JM, et al. Enhanced Infrared Neural Stimulation using Localized Surface Plasmon Resonance of Gold Nanorods. *Small*. 2014:1-5. doi:10.1002/smll.201400599.

46. Paviolo C, Thompson AC, Yong J, Brown WGA, Stoddart PR. Nanoparticle-enhanced infrared neural stimulation. *J Neural Eng*. 2014;11(6):65002. doi:10.1088/1741-2560/11/6/065002.

47. Duke AR, Peterson E, Mackanos MA, Atkinson J, Tyler D, Jansen ED. Hybrid electro-optical stimulation of the rat sciatic nerve induces force generation in the plantarflexor muscles. *J Neural Eng*. 2012;9(6):66006. doi:10.1088/1741-2560/9/6/066006.

48. Duke AR, Cayce JM, Malphrus JD, Konrad P, Mahadevan-Jansen A, Jansen ED. Combined optical and electrical stimulation of neural tissue in vivo. *J Biomed Opt*. 2009;14:60501. doi:10.1117/1.3257230.

49. Duke AR, Lu H, Jenkins MW, Chiel HJ, Jansen ED. Spatial and temporal variability in response to hybrid electro-optical stimulation. *J Neural Eng*. 2012;9(3):36003. doi:10.1088/1741-2560/9/3/036003.

50. Lothet EH, Shaw KM, Lu H, et al. (In Submission) Selective inhibition of small-diameter axons using infrared light. *Sci Rep*. 2017.

51. Ford JB, Jenkins MW, Chiel HJ, Jansen ED. Reducing peak temperatures during infrared inhibition of neural potentials . In: Vol 10052.; 2017:100520B-100520B-7. http://dx.doi.org/10.1117/12.2250019.

52. Welch AJ, Van Gemert MJC. *Optical-Thermal Response of Laser-Irradiated Tissue*.; 2011. doi:10.1007/978-90-481-8831-4.

53. Hale GM, Querry MR. Optical Constants of Water in the 200-nm to 200-microm Wavelength Region. *Appl Opt*. 1973;12(3):555-563. doi:10.1364/AO.12.000555.

54. de Senneville BD, Mougenot C, Quesson B, Dragonu I, Grenier N, Moonen CTW. MR thermometry for monitoring tumor ablation. *Eur Radiol*. 2007;17(9):2401-2410. doi:10.1007/s00330-007-0646-6.

55. Kuroda K. MR techniques for guiding high-intensity focused ultrasound (HIFU) treatments. *Journal of Magnetic Resonance Imaging*. 2017.

56. Rieke V, Pauly KB. MR thermometry. *J Magn Reson Imaging*. 2008;27(2):376-390. doi:10.1002/jmri.21265.

57. Okabe K, Inada N, Gota C, Harada Y, Funatsu T, Uchiyama S. Intracellular temperature mapping with a fluorescent polymeric thermometer and fluorescence lifetime imaging microscopy. *Nat Commun*. 2012;3:705. doi:10.1038/ncomms1714.

58. Tanimoto R, Hiraiwa T, Nakai Y, et al. Detection of Temperature Difference in Neuronal Cells. 2016;6:22071. http://dx.doi.org/10.1038/srep22071.

59. Gardner B, Matousek P, Stone N. Temperature Spatially Offset Raman Spectroscopy (T-SORS): Subsurface Chemically Specific Measurement of Temperature in Turbid Media Using Anti-Stokes Spatially Offset Raman Spectroscopy. *Anal Chem*. 2016;88(1):832-837. doi:10.1021/acs.analchem.5b03360.

60. Lewis MA, Staruch RM, Chopra R. Thermometry and ablation monitoring with ultrasound. *Int J Hyperthermia*. 2015;31(2):163-181. doi:10.3109/02656736.2015.1009180.

61. Incropera FP, DeWitt DP, Bergman TL, Lavine AS. Fundamentals of Heat and Mass Transfer. *Water*. 2007;6th:997. doi:10.1016/j.applthermaleng.2011.03.022.

62. Carpenter DO. Temperature effects on pacemaker generation, membrane potential, and critical firing threshold in Aplysia neurons. *J Gen Physiol*. 1967;50(6):1469-1484. doi:10.1085/jgp.50.6.1469.

63. Rodríguez BM, Sigg D, Bezanilla F. Voltage gating of Shaker K+ channels. The effect of temperature on ionic and gating currents. *J Gen Physiol*. 1998;112(2):223-242. doi:10.1085/jgp.112.2.223.

64. Vandenberg JI, Varghese A, Lu Y, Bursill JA, Mahaut-Smith MP, Huang CL-H. Temperature dependence of human ether-a-go-go-related gene K+ currents. *Am J Physiol Cell Physiol*. 2006;291(1):C165-75. doi:10.1152/ajpcell.00596.2005.

65. Yang F, Zheng J. High temperature sensitivity is intrinsic to voltage-gated potassium channels. *Elife*. 2014;3:e03255. doi:10.7554/eLife.03255.

66. Collins CA, Rojas E. TEMPERATURE DEPENDENCE OF THE SODIUM CHANNEL GATING KINETICS IN THE NODE OF RANVIER. *Q J Exp Physiol*. 1982;67(1):41-55. doi:10.1113/expphysiol.1982.sp002623.

67. Chiel HJ. NeuroWiki: Cable Properties I: Passive Properties. 2016. https://neurowiki.case.edu/wiki/Cable_Properties_I:_Passive_Properties.

68. Hodgkin AL, Huxley AF. A Quantitative Description of Membrane Current and its Application to Conduction and Excitation in Nerves. *J Physiol*. 1952;117:500-544. doi:10.1016/S0092-8240(05)80004-7.

69. Hodgkin AL, Huxley AF, Katz B. Measurement of current-voltage relations in the membrane of the giant axon of *Loligo*. *J Physiol*. 1952;116(4):424-448. doi:10.1113/jphysiol.1952.sp004716.

70. Lu H, Chestek CA, Shaw KM, Chiel HJ. Selective extracellular stimulation of individual neurons

in ganglia. *J Neural Eng*. 2008;5(3):287-309. doi:10.1088/1741-2560/5/3/003.

71. Hovey MM, Bak AF, Carpenter DO. Low internal conductivity of Aplysia neuron somata. *Science*. 1972;176(41):1329-1331. doi:10.1126/science.176.4041.1329.

72. Lucas K. The temperature-coefficient of the rate of conduction in nerve. *J Physiol*. 1908;37(2):112-121. http://www.ncbi.nlm.nih.gov/pmc/articles/PMC1533545/.

73. Hines ML, Carnevale NT. The NEURON Simulation Environment. *Neural Comput*. 1997;9(6):1179-1209. doi:10.1162/neco.1997.9.6.1179.

74. Mou Z, Triantis IF, Woods VM, Toumazou C, Nikolic K. A simulation study of the combined thermoelectric extracellular stimulation of the sciatic nerve of the xenopus laevis: The localized transient heat block. *IEEE Trans Biomed Eng*. 2012;59(6):1758-1769. doi:10.1109/TBME.2012.2194146.

75. Cayce JM, Friedman RM, Chen G, Jansen ED, Mahadevan-Jansen A, Roe AW. Infrared neural stimulation of the primary visual cortex in non-human primates. *Neuroimage*. 2013;84:181-190. doi:10.1016/j.neuroimage.2013.08.040.

76. Wang YT, Rollins AM, Jenkins MW. Infrared inhibition of embryonic hearts. *J Biomed Opt*. 2016;21(6):60505. doi:10.1117/1.JBO.21.6.060505.

77. Lothet EH, Kilgore KL, Bhadra N, et al. Alternating current and infrared produce an onset-free reversible nerve block. *Neurophotonics*. 2014;1:11010. doi:10.1117/1.NPh.1.1.011010.

78. Yoo S, Hong S, Choi Y, Park JH, Nam Y. Photothermal inhibition of neural activity with near-infrared-sensitive nanotransducers. *ACS Nano*. 2014;8(8):8040-8049. doi:10.1021/nn5020775.

79. Wells J, Wells J, Kao C, et al. Application of infrared light for in vivo neural stimulation. *J Biomed Opt*. 2005;10:64002-64003. doi:10.1117/1.2121772.

80. Cayce JM, Friedman RM, Jansen ED, Mahavaden-Jansen A, Roe AW. Pulsed infrared light alters neural activity in rat somatosensory cortex in vivo. *Neuroimage*. 2011;57:155-166. doi:10.1016/j.neuroimage.2011.03.084.

81. De Col R, Messlinger K, Carr RW. Conduction velocity is regulated by sodium channel inactivation in unmyelinated axons innervating the rat cranial meninges. *J Physiol*. 2008;586(4):1089-1103. doi:10.1113/jphysiol.2007.145383.

82. Rao YJ, Webb DJ, Jackson DA, Zhang L, Bennion I. In-fiber bragg-grating temperature sensor system for medical applications. *J Light Technol*. 1997;15(5):779-784. doi:10.1109/50.580812.

83. Ishihara Y, Calderon A, Watanabe H, et al. A precise and fast temperature mapping using water proton chemical shift. *Magn Reson Med*. 1995;34(6):814-823. doi:10.1002/mrm.1910340606.

84. Lothet E, Shaw KM, Horn CC, et al. Selective control of small versus large diameter axons using infrared laser light. In: *Proc. SPIE 9690, Clinical and Translational Neurophotonics; Neural Imaging and Sensing; and Optogenetics and Optical Manipulation*.Vol 96901N. doi:10.1117/12.221294.